

7th Takreer Research Centre Symposium
M. Berthod (Guest editor)

REGULAR ARTICLE

OPEN ACCESS

Refinery processed water treatment *via* the low energy Direct Contact Membrane Distillation (DCMD)

Khadije El Kadi¹, Isam Janajreh^{1,*}, Raed Hashaikeh¹, and Rizwan Ahmed²

¹ Mechanical Engineering Department, Khalifa University of Science and Technology, Masdar Institute, Masdar City, P.O. Box 54224, Abu Dhabi, United Arab Emirates

² ADNOC Refinery Research Center, ADNOC, Abu Dhabi, United Arab Emirates

Received: 23 October 2017 / Accepted: 15 October 2018

Abstract. The amount of refinery water discharged to the environment from oil industry has increased vigorously in current times. Recent research has been focusing on the use of membrane technology for the refinery processed water treatment. Membrane Distillation (MD) is an emerging technology that has been highly marked by its low-energy requirement and high desalination efficiency. However, conventional MD membranes (*i.e.* PVDF) are not feasible for oil-water separation processes. That is due to the oleo-philic property of the membrane and thus, causes membrane fouling and halts the production of mass flux. An anti-oil-fouling membrane is essential for a successful oil-water separation by MD. Underwater-oleophobic as well as omniphobic are two different approaches in fabricating such membranes. The former approach is based on the asymmetric surface wettability, whereas the latter is attributed to the surface structure that is characterized by having a very large contact angle for all liquids. However, such composite membranes are characterized by their lower porosity, smaller pore size, but with unique surface slippage, in comparable with the conventional PVDF membranes. As such, in this work, high fidelity numerical simulation of DCMD is performed using non-isothermal Computational Fluid Dynamics (CFD) validated model in order to assess the role of the anti-oil-fouling membrane properties on the performance of the DCMD. Results are presented in terms of temperature polarization coefficient, mass flux, latent heat flux, and thermal efficiency. Results show the compromising effect of membrane porosity to 45% reduces the mass flux and thermal efficiency respectively by 68% and 40%, and reduction of pore size to the half (*i.e.* 50 nm) can cause a reduction by 50.6% in mass flux and 24.18% in thermal efficiency compared to the baseline (*i.e.* 100 nm). On the other hand, the omniphobic slippage effect leads to a noticeable gain of 16% in DCMD mass flux with slight gain in thermal efficiency. This can maximize mass flux and thermal efficiency to be as much as 50.3 kg/m² h and 69%, respectively.

1 Introduction

Worldwide, oil and gas demand is rising, and the extraction of petroleum products led to large production of oily wastewater. Because the mined crude oil and gas are further refined where large amounts of water are used. Processes like cooling, desalting, flushing, as well as surface water overflow and sanitary wastewater are the different sources of oily wastewater [1]. The final by-product of the refinery process is called the “refinery water” (or processed water) and is characterized by its low dissolved inorganic ions, and high levels of Chemical Oxygen Demand (COD) (*i.e.* 300–800 ppm, and oil content up to 3000 ppm with highly dependency on refinery process complexity [1–3]). Subsequently, refinery water is either disposed, or reused and sometimes as irrigation water. This malpractice causes

a serious environmental stress; thus, it is prominent priorities for petroleum refining industry to remediate water contaminated oil and other suspended solids and chemicals down to marine protection levels which are stipulated by local or international agencies, *i.e.* United States Environmental Protection Agency (USEPA) and Protection of the Marine Environment of the North-East Atlantic (OSPAR) which mandate to be below 42 ppm [4–7].

In UAE, environmental regulation put a limit on oil and grease content of all industrial effluent discharge to the Arabian Gulf of 10 ppm [8, 9]. Current commercial refinery plants do not meet such regulations [1]. Therefore, integrating an effective oil-water separation technology at cost-effective to the refinery process is necessary. Membrane separation is an environmentally friendly and energy-effective technology with higher water quality yield compared with the conventional treatment techniques (*i.e.* biological, chemical, and physical treatments), which

* Corresponding author: ijanjreh@masdar.ac.ae

thought to be suitable for last stage refinery treatment [2, 5, 10–13]. Ultrafiltration (UF), nanofiltration (NF), reverse osmosis (RO), and membrane distillation (MD) are the most pronounced membrane technologies [2]. However, the MD gains more attention by the research community in recent times [14–19], and that is due to its low operating temperatures (*i.e.* 40–70 °C) and nearly 100% rejection of dissolved solids [20]. MD is a thermally driven separation process, where hot feed is cycled on one side of a hydrophobic porous membrane and a cold fresh stream is cycled on the other side. Figure 1 illustrates the Direct Contact Membrane Distillation (DCMD) system at its simplest configuration.

A non-wetting hydrophobic membrane is the principle component for a successful MD [2]. Though, the presence of oil and other organic compounds in the refinery processed water form obstacles and halt the operation of MD. These contents cause wetting and result in the blockage of the membrane pores, thus cause membrane fouling and minimize the permeation flux as shown in Figure 2 [21, 22].

Conventional MD membranes are non-oleophobic and thus, are not feasible for oily-water feed. Extensive studies have been conducted lately focusing on improving membrane's surface properties concerning oil-water separation application [22–29]. Generally, there are two major approaches to improve membrane's anti-oil-fouling: (i) hydrophilic/hydrophobic composite membrane, and (ii) omniphobic/hydrophobic composite membrane [22, 23, 25, 26, 30]. Where the key element of both compositions is to reduce the adhesion of oil on the membrane surface thereby reduces fouling and improves fresh water productivity [30].

The first approach is based on underwater oleophobic low-energy surfaces which have been developed recently [24, 31, 32]. Referring to Young's relation of wettability [33], these surfaces are typically hydrophilic once they are exposed to an air medium. For oil-water separation MD, this explains the necessity of having a double-layer composite membrane with unequal wettability of an upper layer of underwater-oleophobic surface followed by a hydrophobic layer. However, such composition leads to pore size reduction [22], and may risk wetting [34]. This is attributed to the possibility of coating the inner pores of the underneath hydrophobic layer with the hydrophilic coating. Titanium oxide, cellulose, Fluorosurfactant are some examples of hydrophilic surface coating. Tabulated summary review is illustrated in Table 1.

On the other hand, the second approach of obtaining an anti-oil-fouling membrane is based on the omniphobic materials, which are capable of repelling water or any other liquids with low surface tension (*i.e.* oil) [25, 26]. Using this material ensures thermodynamic equilibrium of liquid-solid-vapor interface and satisfies the Cassie-Baxter state [26, 35]. These omniphobic surfaces have the ability of creating a strong interface with apparent contact angle of greater than 150° regardless of the contacting liquid's surface tension [35]. Moreover, omniphobic surfaces induce liquid slip on the boundary of membrane surface [36]. This is accredited to the dual micro/nano structure of the Cassie-Baxter state,

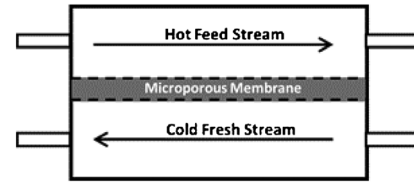


Fig. 1. Schematic diagram of the DCMD counter flow configuration.

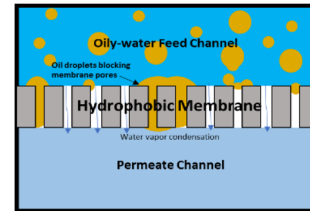


Fig. 2. Schematic showing the blockage of membrane pore due to the hydrophobic-hydrophobic interaction between oil droplets and the membrane.

as well as to the low surface energy coating [36, 37]. Liquid slip, indeed, has a favorable effect on both momentum and heat flow in microchannel applications.

From literature (see Table 1), it is noticeable that all anti-oil-fouling membranes cause the flux to drop sharply due to the change in membrane properties. Thus, an extensive study on the influence of these membranes (*i.e.* pore size and porosity as well as the operational conditions *i.e.* slip *vs.* no-slip, and Re) on the MD performance is done in this work using an experimentally-validated non-isothermal Computational Fluid Dynamics (CFD) and thermally coupled model of DCMD targeting oil/water separation.

2 Scope of work

2.1 Numerical model and governing equations

In this work, a numerical study will be performed on Direct Contact Membrane Distillation (DCMD) using non-isothermal Computational Fluid Dynamics (CFD) coupled thermally with the solid porous membrane. Dimensions of 210 mm length and 1 mm height per channel with a 0.13 mm sandwiched membrane has been adopted for the DCMD module simulation. A schematic of the system setup in counter current flow is illustrated in Figure 3.

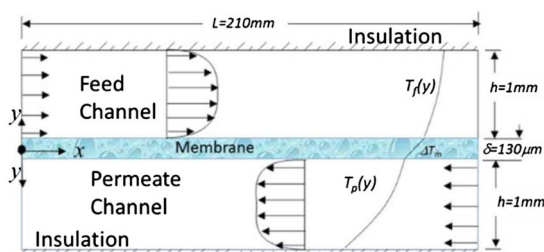
A symmetrical 2D flow system is discretized as shown in Figure 4. Using a structured quadrilateral mesh type and reasonable resolution to capture the wall boundary layer. This mesh size is 2100 × 64 per channel and 2100 × 8 for the membrane. The governing equations for the system are the conjugated steady incompressible Navier-Stokes and energy equations, and are written as:

Continuity:

$$\frac{\partial \rho U}{\partial x} + \frac{\partial \rho V}{\partial y} = 0. \quad (1)$$

Table 1. Summary of prominent work done on approaching anti-oil-fouling composite membranes.

Author	Approach	Findings
• Zuo and Wang [22]	• <i>Hydrophilic/hydrophobic composite membrane</i> Polyethylene glycol + TiO ₂ deposition on PVDF by plazma grafting	• Pore size reduction from 0.55 μm to 0.27 μm • CA for water decreased from 120° to 25.2° • Stable flux observed (6.3 L/m ² h) • 13% flux reduction to the baseline PVDF
• Wang and Lin [23]	• <i>Underwater-oleophobic/hydrophobic composite</i> (FS/CTS/PFO-PVDF)	• Stable in-air CA: 139.6°, in-water CA < 90° (hydrophilic) • Sharp reduction in permeate flux (31 L/m ² h for PVDF to 0.49 L/m ² h for FS/CTS/PFO-PVDF)
• Lee et al. [25]	• <i>Omniphobic composite membrane</i> Electrospun BTEAC/PVDF-HFP coated with SiNPs	• Reduction of pore size from 2.23 μm for PVDF-HFP to 0.42 μm for BTEAC/PVDF-HFP • Water CA of ~150° • Stable flux and salt rejection
• Lin et al. [26]	• <i>Omniphobic composite membrane</i> APTES-coated GF with (-ve) charged SiNPs suspension treated with fluorinated alkyl silane (FAS)	• High water CA (≈140°) • High oil CA (≈100°) • 100% salt rejection • Low flux of 2.7 L/m ² h (32.6 L/m ² h for PTFE)
• Wang et al. [27]	• <i>Underwater-oleophobic/hydrophobic composite</i> (CTS-PFO/SiNPs) Silica nanoparticles-polymer coating on PVDF substrate	• Composite membrane porosity of 72.5% and pore size 388 nm, compared to 75% and 392 nm for the baseline PVDF • 4% membrane thickness increase • in-air water CA: 0°, underwater oil CA: 149.5° • Stable flux with initial value of 26.15 L/m ² h
• Ahmed et al. [29]	• <i>Hydrophilic/hydrophobic composite</i> Cellulose electrospun PVDF-HFP composite membrane	• Pore size reduction from 0.92 μm to 0.3 μm • Porosity reduction from 91% to 35% • PVDF hydrophobic: water CA 130°, Cellulose/PVDF composite: oil CA of 169° and 0° for water • 90%–99% of oil separation efficiency achieved • Flux of 1781 L/m ² h bar

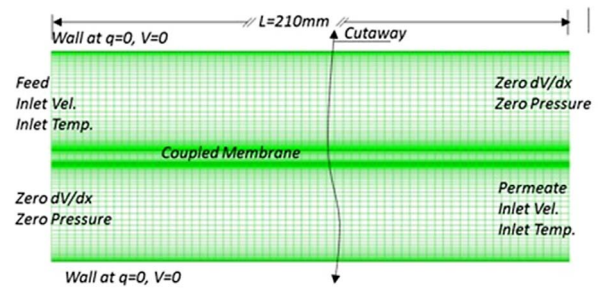
**Fig. 3.** Schematic of counter flow configuration for the DCMD.

x -Momentum:

$$U \frac{\partial \rho U}{\partial x} + V \frac{\partial \rho U}{\partial y} = -\frac{\partial P}{\partial x} + \mu \left(\frac{\partial^2 U}{\partial x^2} + \frac{\partial^2 U}{\partial y^2} \right). \quad (2)$$

y -Momentum:

$$U \frac{\partial \rho V}{\partial x} + V \frac{\partial \rho V}{\partial y} = -\frac{\partial P}{\partial y} + \mu \left(\frac{\partial^2 V}{\partial x^2} + \frac{\partial^2 V}{\partial y^2} \right) + \rho g_y. \quad (3)$$

**Fig. 4.** 2D DCMD numerical model setup and discretized mesh.

Energy:

$$U \frac{\partial \rho C_p T}{\partial x} + V \frac{\partial \rho C_p T}{\partial y} = k \left(\frac{\partial^2 T}{\partial x^2} + \frac{\partial^2 T}{\partial y^2} \right) + S_h, \quad (4)$$

where U and V are the velocity components, ρ is the density, μ is the viscosity, P is the pressure, g_y is the gravitational acceleration, T is the temperature, C_p is the specific heat, k is the thermal conductivity, and S_h is the sink/source additional heat.

Boundary conditions are imposed by the flow inlet and wall Dirichlet conditions (prescribed velocity and temperature value) and outlet zero-velocity gradient and constant atmospheric pressure Neumann conditions (zero gradient). In the baseline case, walls are subjected to no-slip and no penetrating velocity. However, a sensitivity study on slip B.C. is done in this work and will be further explained. Thermally, membrane walls are coupled while outer walls of both channel are insulated (Neumann of zero gradient, *i.e.* zero heat flux). These boundary conditions are summarized in [Table 2](#). A cutaway of the established baseline mesh and the computational domain boundary conditions are shown in [Figure 4](#).

Reynolds number of 10 and 100 are set for the flow conditions for a brine/feed and fresh/permeate are set at. This is equivalent to prescribed velocity of 0.01 m/s and 0.1 m/s, respectively. The feed temperature is at 75 °C, whereas the permeate is at 25 °C. The solution is carried by FLUENT commercial CFD code that based on finite volume approach and segregated solver. The Semi-Implicit Method for Pressure-Linked Equations (SIMPLE) algorithm is used for pressure-velocity coupling and second order upwind spatial derivatives. Convergence residual is set very tight of $1E10^{-15}$ for continuity equation, and $1E10^{-3/-6}$ for x - and y -momentums, and energy equations.

Because of the thermally coupled membrane, the temperature distribution at the top and bottom membrane surfaces is the most pronounced flow variable. As the temperature and velocity field are computed, performance metrics including temperature polarization coefficient, mass flux, and thermal efficiency will be assessed. Furthermore, number of sensitivity studies on membrane properties using the developed model. This includes varying (i) membrane porosity in a range between 45% and 85%, (ii) pore size between 50 nm and 200 nm, and finally (iii) simulating the slippage (*i.e.* zero shear stress) effect of the omniphobic membrane. These studies are carried out to assess the MD performance for oily wastewater treatment as the case in refinery water. All sensitivity studies are done independently by fixing all other parameters.

2.2 DCMD experimental setup

Experimental work is limited by obtaining the overall system performance, however, high fidelity modeling offers both macro- and micro-scale visualization. The experimental setup shown in [Figure 5](#) is developed to validate the numerical model using suitable MD membrane being commercially available or internally developed. This experimental setup consists of DCMD acrylic model of flat-sheet type of two symmetrical rectangular channels that are separated by the PVDF membrane of known properties per [Table 3](#). Both the experimental module and numerical model are identical. The flow to these channels is driven by two peristaltic pumps that inject a steady laminar flow at the stipulated rate and temperature by mean of thermal heat control in each channel reservoir. Each channel is instrumented by 18 T-Type thermocouples at an equally distributed distance to record the fluid temperature. The system is fed by two thermal reservoirs that are kept at

Table 2. Boundary conditions model assignments.

Boundary	Velocity	Temperature	Pressure
Feed inlet	V_f	T_f	Un-prescribed
Feed outlet	$dv/dx = 0$	$dT/dx = 0$	$P = 0$
Perm. inlet	V_f	T_f	Un-prescribed
Perm. outlet	$dV/dx = 0$	$dT/dx = 0$	$P = 0$
Bulk walls	$V = U = 0$	$dT/dy = 0$	Un-prescribed
Memb. walls	$V = U = 0$	Coupled	Un-prescribed

fixed temperature. The flux is measured by an overflowing graded flask which connect to the permeate reservoir.

3 System metrics

3.1 Mass flux

Due to temperature polarization, the saturated pressure gradient across membrane surfaces occurs and drives the mass transfer through the hydrophobic porous membrane. The general mass flux expression is as follows [\[39, 40\]](#):

$$J'' = c_m \left(P_f^{\text{sat}} - P_p^{\text{sat}} \right), \quad (5)$$

where c_m is the membrane mass coefficient and P_f^{sat} and P_p^{sat} are the saturated water vapor pressures at the feed and permeate membrane surface, respectively. The vapor pressure of pure water and its temperature relationship is estimated using the Antoine equation [\[41\]](#) and tabulated in steam tables. Adjustment is relationship is estimated using the Antoine equation [\[41\]](#) and tabulated in steam tables. Adjustment is required for binary mixtures (*i.e.* saline and multiple specie solutions or waste-water) as per the work of [\[17–19, 40\]](#).

Three essential membrane coefficient models are stated in literature to describe the mass transfer across the microporous hydrophobic membrane [\[40\]](#): (i) the Knudson model, (ii) the Poiseuille flow model, and (iii) the molecular diffusion model. At small pore size as the current case, the diffusion model can be ignored without compromising the results [\[40\]](#). However, in this work a combination of Knudson and Poiseuille models is used simultaneously following the work of Chen *et al.* [\[40\]](#) and is described by:

$$c_m = c_K + c_P \\ = 1.064\alpha(T) \frac{\varepsilon r_p}{\tau \delta_m} \sqrt{\frac{M_w}{RT_m}} + 0.125\beta(T) \frac{\varepsilon r_p^2}{\tau \delta_m} \frac{M_w P_m}{RT_m \mu_v}, \quad (6)$$

where $\alpha(T)$, and $\beta(T)$ are Knudsen diffusion model and Poiseuille flow model contributions, respectively. M_w is molar mass of the water in kg/mol, T_m is mean membrane temperature (°C), R is gas constant, P_m is mean pressure, δ_m thickness of the membrane, μ_v is gas viscosity, r_p is pores radius, ε is the membrane porosity, and τ is tortuosity factor.

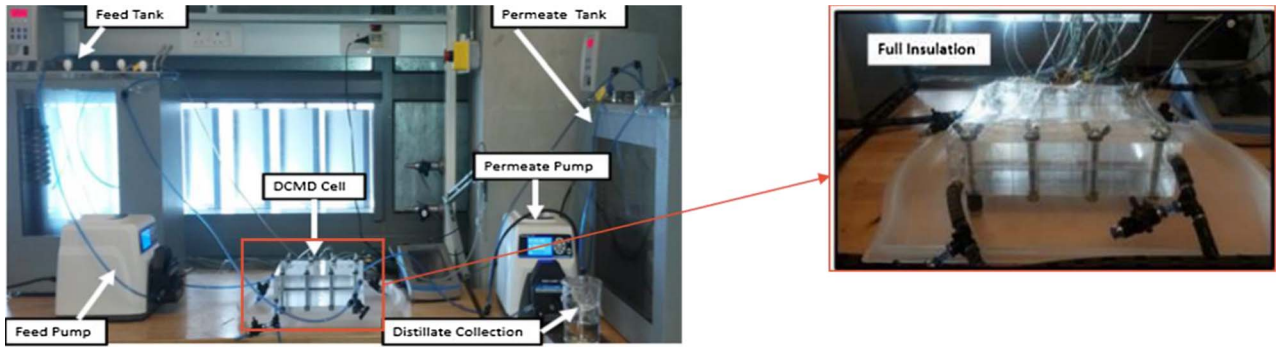


Fig. 5. DCMD flat sheet laboratory setup.

Table 3. Properties of the bulk PVDF material, vapor, and PVDF porous membrane, respectively.

Material	Density (kg/m ³)	Specific heat (J/kg K)	Conductivity (W/m K)
PVDF [38]	1,175	1,325	0.2622
Vapor	0.554	2,014	0.0261
Membrane	302.2	1896.9	0.0662

3.2 Heat flux

The heat transfer in DCMD can be described in a series of three thermal resistances: (i) Convective transfers through the feed boundary layer, (ii) Combined transfer across the membrane, and finally (iii) Convective transfer through the permeate boundary layer [16]. The total heat flux across the membrane (Q_m) is attributed to a combination of the conduction (Q_c) and latent heat of evaporation (Q_v) and expressed as:

$$Q_m = Q_c + Q_v, \quad (7)$$

where the conduction part is due to the bulk membrane material, while the evaporation takes place in the membrane pores. Taking ΔH_m to be the enthalpy change due to the latent heat of the transmembrane mass flux, it can be written as described by Termpiyakul *et al.* as [42]:

$$Q_v = J'' \Delta H = J'' (H_{m,f} - H_{m,p}). \quad (8)$$

The conductive heat flux fraction is described by Fourier heat equation as:

$$Q_c = -\frac{k_m}{\delta_m} (T_{m,f} - T_{m,p}), \quad (9)$$

where k_m is the equivalent thermal conductivity of the membrane and is due to the bulk conductivity (k_b) and the vapor conductivity (k_g) of the weighted volume average. The subscripts f and p signify the feed and permeate, respectively.

3.3 Thermal efficiency and TPC

Thermal efficiency represents the fraction of the heat used as latent heat of evaporation to the total heat flux of equation (7) and is described as:

$$\eta = \frac{Q_v}{Q_m} = \frac{J'' \Delta H_m}{Q_m}, \quad (10)$$

where the denominator accounts for the total heat transfer that include both latent heat flux as per equation (7). In the other hand, temperature polarization coefficient (TPC or θ) defines the ratio of membrane boundary layer resistance over the total/bulk heat transfer resistance and is expressed as:

$$\theta = \frac{T_{m,f} - T_{m,p}}{T_{b,f} - T_{b,p}} = \frac{\Delta T_m}{\Delta T_b}, \quad (11)$$

where the subscripts m , b , f , p indicate the membrane, bulk, and feed and permeate surfaces, respectively. A small value of θ (≤ 0.2) signifies a limited heat transfer DCMD system [17–18, 43].

4 Results and discussion

4.1 Model validation

Model is validated initially by comparing the measuring and the simulated temperature along the membrane and bulk surfaces. After few minutes of setting the flow, the DCMD system arrives into steady state operation. Both the experimental and simulation are conducted at similar conditions (*i.e.* counter flow configuration, $Re = 40$, inlet feed at 50 °C, inlet permeate at 25 °C). The values of the thermocouples located along the length of the DCMD module and their corresponding locations numerical results are illustrated in Figure 6a. Moreover, TPC values (per Eq. (11)) are also compared for both models as depicted in Figure 6b. A strong agreement between both experimental and numerical results is clearly noticed suggesting good fidelity of the model.

Additionally, a well-behave system can be seen clearly in the temperature contours and velocity vectors of the

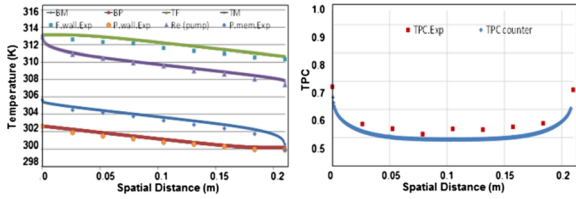


Fig. 6. Experimental and numerical temperature distributions (a) and TPC (b) of the DCMD model.

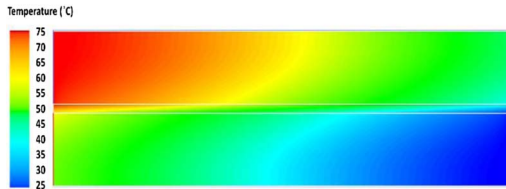


Fig. 7. Temperature contours of DCMD numerical model running at counter flow with 75 °C and 25 °C inlet temperatures of feed and permeate channels respectively, and $Re = 10$ (y -axis is scaled up for better visualization).

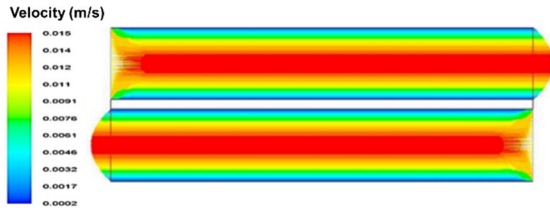


Fig. 8. Velocity vectors of DCMD numerical model running at counter flow with 75 °C and 25 °C inlet temperatures of feed and permeate channels respectively, and $Re = 10$ (y -axis is scaled up for better visualization).

numerical model as depicted in Figures 7 and 8, respectively. This temperature distribution illustrates the thermally coupled membrane as well as the insulated walls. Moreover, counter flow configuration with no-slip B.C. is clearly represented in the velocity vectors. Furthermore, Figure 9 shows the numerical model TPC distribution at different Reynolds numbers (*i.e.* 10 and 100). As such, all the past results ensure validation of the numerical model which gives enough confidence to run several sensitivity studies.

4.2 Membrane porosity sensitivity study

As part of studying the effect of the two approaches of anti-oil-fouling membranes on the DCMD performance, role of porosity is studied in this section. A post processing modification is done using different values of porosity (*i.e.* 85%, 80%, 75%, 60%, and 45%) where typical PVDF membranes have a porosity of 75–85%. It is worth mentioning that pore size was fixed in all cases of this study to 100 nm. A significant reduction in the DCMD performance metrics was observed at low porosity values. For instance,

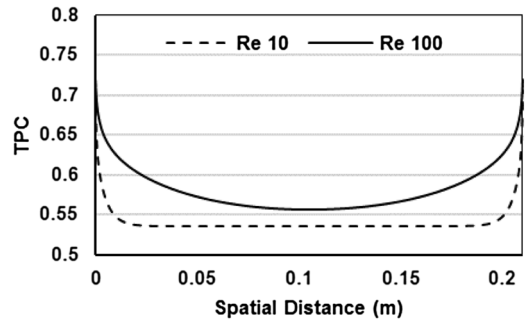


Fig. 9. TPC distribution of DCMD model at different Re numbers, high Re shows better TPC performance.

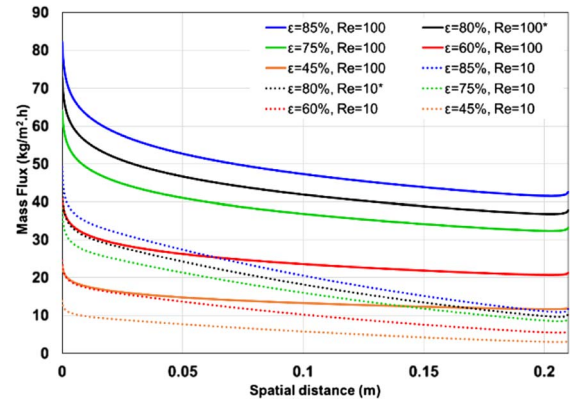


Fig. 10. Mass flux distribution along the DCMD spatial at different Re and porosity values (*baseline).

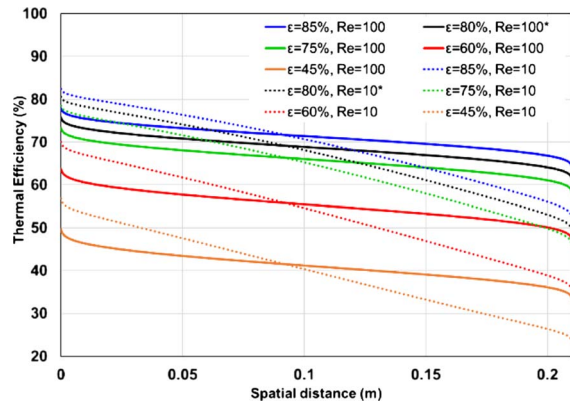


Fig. 11. Thermal efficiency distribution along the DCMD spatial at different Re number and porosity values (*baseline).

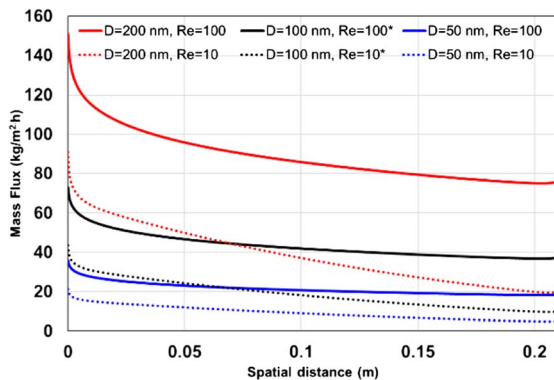
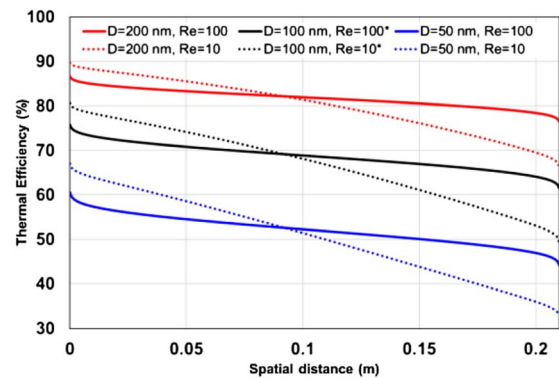
reducing the porosity by 35% (*i.e.* from 80% to 45%) leads to mass flux and thermal efficiency loss by 68% and 40%, respectively. This sharp reduction is attributed to the lower c_m (or mass coefficient) as this parameter is nearly quadratically and directly proportional to the porosity. The reduction of porosity typically leads also to an increase in tortuosity. It is obvious that the less porosity the more the membrane gets denser, which as a result leads

Table 4. Quantitative DCMD system metrics summary for different sensitivity studies on membrane properties (at $Re = 100$, and $75\text{ }^\circ\text{C}$ feed temperature).

Parameter	Growth/reduction factor	Average mass flux, J' ($\text{kg}/\text{m}^2\text{ h}$)		Average thermal efficiency, η (%)	
		J'	Loss/gain (%)	η	Loss/gain (%)
Porosity*					
85%	1.0625	48.89	+12.91	71.23	+3.7
80%	1	43.30	Baseline	68.69	Baseline
75%	0.9375	38.06	-12.10	65.86	-4.12
60%	0.75	24.36	-43.74	55.29	-19.51
40%	0.5	13.70	-68.36	41.08	-40.20
Pore size**					
200 nm	2	88.69	+104.8	81.75	+19.01
100 nm	1	43.30	Baseline	68.69	Baseline
50 nm	0.5	21.39	-50.6	52.08	-24.18
Superhydrophobicity***					
No-slip	-	43.30	Baseline	68.69	Baseline
Slip	-	50.27	+16.10	69.03	+0.49

*At $0.1\text{ }\mu\text{m}$ pore size.

**At 80% porosity.

***At $0.1\text{ }\mu\text{m}$ pore size, 80% porosity.**Fig. 12.** Mass flux distribution along the DCMD spatial at different Re number and pore size (D) (*baseline).**Fig. 13.** Thermal efficiency distribution along the DCMD spatial at different Re number and pore size (D) (*baseline).

to increase heat loss potential by conduction, and thus, a reduction in thermal efficiency. The directly proportional relationship between mass flux and porosity as well as between thermal efficiency and porosity is well demonstrated in Figures 10 and 11, respectively. Table 4 quantifies system performance in terms of averaged mass and latent heat fluxes, and thermal efficiency at the different porosity values along with the associated loss/gain percentages.

4.3 Pore size sensitivity study

It was also clarified from literature that anti-oil-fouling membranes of both approaches attribute to a significant apparent pore size reduction when compared to the baseline hydrophobic PVDF membrane. This is attributed to the

composite structure of the membrane, where a second layer material is coated on the PVDF substrate. This sensitivity study carries out the effect of reducing the pore size to the half (from 100 nm to 50 nm) and the effect of doubling it (from 100 nm to 200 nm) on the DCMD performance. Like porosity, smaller pore size also reduces the c_m but is linearly and directly proportional. It is clear from Figures 12 and 13 the sharp reduction (*i.e.* $\sim -50\%$ and $\sim -25\%$) of both mass flux and thermal efficiency, respectively. This is simply because of reducing transmembrane vapor paths and thus reduces mass flux. Moreover, low thermal efficiency is translated into higher heat losses by conduction due to higher mass fraction of solid polymeric material at lower pore size. Noting that porosity was fixed at 80% in this study for both pore sizes. More detailed quantification of system performance is illustrated in Table 4.

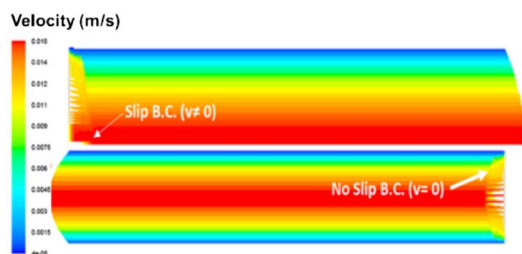


Fig. 14. Slippage effect illustration in the DCMD velocity vectors ($Re = 100$, y -axis scaled by 15).

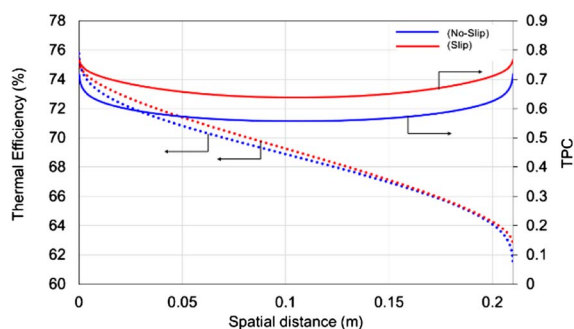


Fig. 15. TPC and thermal efficiency distributions along the DCMD spatial under slip *vs.* no-slip effects at the membrane surface ($Re = 100$).

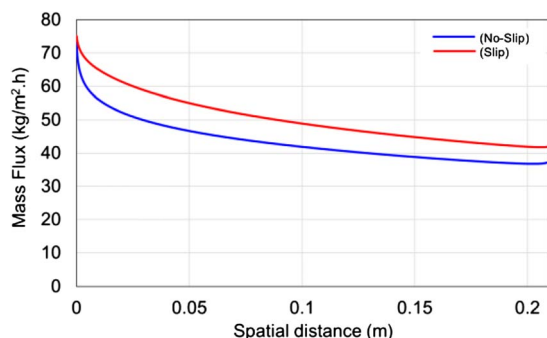


Fig. 16. Mass flux distribution along the DCMD spatial under slip *vs.* no-slip effects at the membrane surface ($Re = 100$).

4.4 Omniphobic slippage sensitivity study

Top membrane boundary condition was modified to have zero-shear stress and induce slippage to simulate the omniphobic effect. As illustrated in Figure 14 and compared to Figure 8, velocity profile of the feed channel is no longer parabolic and a maximum velocity of 0.015 m/s can be obtained at top membrane surface. The temperature difference across membrane surfaces is noticeably higher when slip condition is applied, which leads to higher polarization (see Fig. 15) and thus, higher driving pressure. Although a drop of the TPC profile at feed outlet occurs (at $x = 0.21$ m) due to the slip condition, a rise in the average

slip TPC (~ 0.67) in comparable to the no-slip (~ 0.58) can be obtained.

Furthermore, results of thermal efficiency distributions along DCMD module for both boundary conditions (*i.e.* no-slip and slip) are well-depicted in Figures 15 and 16, respectively. Applying slippage effect of the omniphobic membrane can lead to a gain of $\sim 16\%$ on the averaged mass flux, whereas a negligible gain (*i.e.* $\sim 0.5\%$) is observed for thermal efficiency. Summary of the attained system metrics along with their relative gain percentages are tabulated in Table 4.

5 Conclusion

This work addressed the DCMD performance applied to the oil and gas industry processed water. As this water contains high amount of oil and grease, conventional DCMD membranes are not suited for oil-water separation. Composite oleophobic/hydrophobic or omniphobic/hydrophobic membranes thought to be the suited technology for refinery oil/water separation. This however comes at a compromise in membrane properties (*i.e.* lower porosity and pore size) when targeting this industry.

Studies were carried out by a validated numerical-based CFD model at different sensitivity studies on anti-oil-fouling membranes. The model was generic to accommodate different membrane properties and operational parameters and hence, quantifying their impacts on MD performance. Anti-oil-fouling membranes were found to halt MD system metrics significantly. However, around 16% gain in system metrics were observed when simulating the slip feature of omniphobic surface. Low temperature grades of the MD process give it the priority of using such technology in refinery water treatment. Still, there are more work needed to target oily water as far as the two stated approaches of membrane fabrication.

Acknowledgments. The partial sponsorship of Masdar Institute and Takreer Research center in Abu Dhabi, UAE is highly acknowledged.

References

- 1 Al Zarooni M., Elshorbagy W. (2006) Characterization and assessment of Al Ruwais refinery wastewater, *J. Hazardous Mater.* **A136**, 398–405.
- 2 Munirasu S., Abu Haija M., Banat F. (2016) Use of membrane technology for oil field and refinery produced water treatment – a review, *Process Safety Env. Protection* **100**, 183–202.
- 3 Dold P.L. (1989) Current practice for treatment of petroleum refinery wastewater and toxics removal, *Water Qual. Res. J.* **24**, 3, 363–390.
- 4 Ahmadun F.R., Pendashteh A., Abdullah L., Biak D., Madaeni S., Zainal Z.Z. (2009) Review of technologies for oil and gas produced water treatment, *J. Hazardous Mater.* **170**, 2–3, 530–551.
- 5 Neff J.M. (2002) *Bioaccumulation in marine organisms*, Elsevier, Netherlands.

- 6 U.S. Environmental Protection Agency, <http://www.epa.gov>
- 7 OSPAR Commission (2005) *Report on discharges spills and emissions from offshore oil and gas installations*, ISBN 1-904426-60-3, Publication Number: 2005/221.
- 8 PCFC-Trakhees (2013) *Regulation EN 5. 0 - Water Environment*, Dept. of Planning & Dev., Dubai Gov., www.trakhees.ae.
- 9 Carter N. (2010), *Trade Effluent Control Regulations*, Abu Dhabi Regulation & Supervision Bureau, 48 p.
- 10 Cabassud C., Anselme C., Bersillon J.L., Aptel P. (1991) Ultrafiltration as a nonpolluting alternative to traditional clarification in water treatment, *Filtration and Separation* **28**, 3, 194–198.
- 11 Madaeni S.S. (1999) Review paper: The application of membrane technology for water disinfection, *Water Res.* **33**, 2, 301–308.
- 12 Regunathan P., Beauman W.H., Kreusch E.G. (1983) Efficiency of point-of-use treatment devices, *J. Am. Water Works. Ass.* **75**, 1, 42–50.
- 13 Maab H., Francis L., Al-Saadi A., Aubry C., Ghaffour N., Amy G., Nunes S.P. (2012) Synthesis and fabrication of nanostructured hydrophobic polyazole membranes for low-energy water recovery, *J. Membr. Sci.* **423–424**, 11–19.
- 14 Alkhudhiri A., Darwish N., Hilal N. (2012) Membrane distillation: A comprehensive review, *Desalination* **287**, 2–18.
- 15 Alklaibi A., Lior N. (2006) Heat and mass transfer resistance analysis of membrane distillation, *J. Membr. Sci.* **282**, 1–2, 362–369.
- 16 Khayet M. (2011) Membranes and theoretical modeling of membrane distillation: A review, *Adv. Colloid Interface Sci.* **164**, 56–88.
- 17 Janajreh I., Suwwan D. (2014) Numerical simulation of Direct Contact Membrane Desalination (DCMD): II, *Int. J. Eng. Res. Innov.* **6**, 2, 21–33.
- 18 Janajreh I., Suwwan D., Hashaikeh R. (2017) Assessment of direct contact membrane distillation under different configurations, velocities, and membrane properties, *Appl. Energy* **185**, 2058–2073.
- 19 Janajreh I., El Kadi K., Hashaikeh R., Ahmed A. (2017) Numerical investigation of air gap membrane distillation (AGMD): Seeking optimal performance, *Desalination* **424**, 122–130.
- 20 Lawson K.W., Lloyd D.R. (1996) Membrane distillation. II. Direct contact MD, *J. Membr. Sci.* **120**, 123–133.
- 21 Liu F., Hashim N.A., Liu Y., Abed M.R. (2011) Progress in the production and modification of PVDF membranes, *J. Membr. Sci.* **375**, 1–2, 1–27.
- 22 Zuo G., Wang R. (2013) Novel membrane surface modification to enhance anti-oil fouling property for membrane distillation, *J. Membr. Sci.* **447**, 26–35.
- 23 Wang Z., Lin S. (2017) The impact of low-surface-energy functional groups on oil fouling resistance in membrane distillation, *J. Membr. Sci.* **527**, 68–77.
- 24 Kwon G., Post E., Tuteja A. (2015) Membrane with selective wettability for the separation of oil-water mixtures, *MRS Commun.* **5**, 475–494.
- 25 Lee J., Boo C., Ryu W.H., Taylor A., Elimelech M. (2016) Development of omniphobic desalination membranes using a charged electrospun nanofiber scaffold, *ACS Appl. Mater. Interfaces* **8**, 17, 11154–11161.
- 26 Lin S., Nejati S., Boo C., Hu Y., Osuji C., Elimelech M. (2014) Omniphobic membranes for robust membrane distillation, *Env. Sci. Tech. Lett.* **1**, 443–447.
- 27 Wang Z., Hou D., Lin S. (2016) Composite membrane with underwater-oleophobic surface for anti-oil-fouling membrane distillation, *Env. Sci. Tech.* **50**, 7, A-I.
- 28 Barnett S.M. (2001) Oil/water separation using nano-filtration membrane technology, *Sep. Sci. Technol.* **36**, 1527–1542.
- 29 Ahmed F., Laila B., Hilal N., Hashaikeh R. (2014) Underwater superoleophobic cellulose/electrospun PVDF-HFP membranes for efficient oil/water separation, *Desalination* **344**, 48–54.
- 30 Padaki M., Murali S., Abdullah M.S., Misdan N., Moslehyani A., Jassim M.A., Hilal N., Ismail A.F. (2015) Membrane technology enhancement in oil-water separation. A review, *Desalination* **357**, 197–207.
- 31 Wang Z., Jiang X., Cheng X., Lau C.H., Shao L. (2015) Mussel-inspired hybrid coatings that transform membrane hydrophobicity into high hydrophilicity and underwater superoleophobicity for oil-in-water emulsion separation, *ACS Appl. Mater. Interfaces* **7**, 9534–9545.
- 32 Liu M.J., Wang S.T., Wei Z.W., Song Y.L., Jiang L. (2009) Bioinspired design of a super-oleophobic and low adhesive water/solid interface, *Adv. Mater.* **21**, 665.
- 33 Young T. (1805) An essay on the cohesion of fluids, *Phil. Trans. R. Soc.* **95**, 65.
- 34 Guillen-Burrieza E., Mavukkandy M.O., Bilad M.R., Arafat H.A. (2016) Understanding wetting phenomena in membrane distillation and how operational parameters can affect it, *J. Membr. Sci.* **515**, 163–174.
- 35 Tuteja A., Choi W., Mabry J., McKinley G., Cohen R. (2008) Robust omniphobic surfaces, *Proc. Natl. Acad. Sci.* **105**, 47, 18200–18205.
- 36 Wu Y., Cai M., Li Z., Song X., Wanf H., Pei X. (2014) Slip flow of diverse liquids on robust superomniphobic surfaces, *J. Colloid Interface Sci.* **414**, 9–13.
- 37 Lee D., Cho K., Jang S., Song Y., Youn J. (2012) Liquid slip on nanostructured surface, *Langmuir* **28**, 10488–10494.
- 38 Iguchi C.Y., dos Santos W.N., Gregorio R. (2007) Determination of thermal properties of pyroelectric polymers, copolymers and blends by the laser flash technique, *Polym. Test.* **26**, 6, 788–792.
- 39 Pangarkar B.L., Sane M.G. (2011) Heat and mass transfer analysis in air gap membrane distillation process for desalination, *Membr. Water Treat.* **2**, 3, 159–173.
- 40 Chen T.-C., Ho C.-D., Yeh H.-M. (2009) Theoretical modeling and experimental analysis of direct contact membrane distillation, *J. Membr. Sci.* **330**, 1–2, 279–287.
- 41 Felder R.M., Rousseau R.W. (2000) *Elementary principles of chemical processes*, 3rd edn., John Wiley & Sons, New York.
- 42 Termpiyakul P., Jiraratananon R., Srisurichan S. (2005) Heat and mass transfer characteristics of a direct contact membrane distillation process for desalination, *Desalination* **177**, 1–3, 133–141.
- 43 Záarate J.M., Velázquez A., Peña L., Mengual J.I. (1993) Influence of Temperature Polarization on Separation by Membrane Distillation, *Sep. Sci. Technol.* **28**, 7, 1421–1436.